BioNanoScience (2023) 13:2134–2150
https://doi.org/10.1007/s12668-023-01180-4

Analysis of MHD Bioconvection Flow of a Hybrid Nanofluid Containing Motile Microorganisms over a Porous Stretching Sheet

Shiva Rao[1] · **P.N. Deka**[1]

Accepted: 7 August 2023 / Published online: 15 August 2023

Abstract

This paper presents a numerical investigation of steady two-dimensional bioconvective MHD flow along with the heat and mass transfer phenomena of a water-based hybrid nanofluid containing motile microorganisms over a porous stretching sheet. The study considers effects of various physical parameters, such as thermal radiation, chemical reactions, Joule heating, and heat generation, on the flow and transport characteristics of the system. Copper (Cu) and alumina (Al_2O_3) nanoparticles are used with water (H_2O) as the base fluid. The governing equations are transformed into a set of nonlinear ordinary differential equations using a standard similarity transformation. The reduced equations are solved numerically using the Keller-box method. The impact of different parameters on the velocity, temperature, concentration, and microorganism concentration profile is illustrated graphically, while their influence on the skin-friction coefficient, local Nusselt number, local Sherwood number, and local density number of motile microorganisms is tabulated. This study provides an excellent agreement with previously published works. The results of the study show that the presence of motile microorganisms significantly enhances the heat transfer rate and mixing efficiency of the nanofluid. The analysis demonstrates that the chemical reaction and thermal radiation play crucial roles in controlling the concentration and temperature distributions of the nanofluid, respectively.

Keywords Thermal radiation · Chemical reactions · Stretching sheet · Hybrid nanofluid · Motile microorganism · Joule heating

Nomenclature

a, b	Constant
x, y	Cartesian coordinates along the surface and normal to it, respectively (m)
u, v	Velocity component along x-axis and y-axis respectively (m s^{-1})
T	Temperature (K)
C	Nanoparticle concentration (mol l^{-1})
N	Concentration of the microorganism
B_o	Magnetic field (T)
k_o	Porous term (m^2)
Q_o	Coefficient of heat generation
C_p	Specific heat at constant pressure (J kg^{-1} K^{-1})
q_r	Radiative heat flux
D_m	Mass diffusion coefficient
D_n	Microorganisms' diffusion coefficient
Kr	First-order chemical reaction coefficient
W_c	Maximum cell swimming speed
k^*	Mean absorption coefficient
M	Magnetic parameter
Ec	Eckert number
Q	Heat generation/absorption
K_p	Permeability parameter
Pr	Prandtl number
Rd	Radiation parameter
Sc	Schmidt number
Sb	Bioconvection Schmidt number
Pe	Bioconvection Peclet number
Cf_x	Skin-friction coefficient
Nu_x	Nusselt number
Sh_x	Sherwood number
Nn_x	Density number of motile microorganism
Re_x	Reynold number

Greek symbols

ν	Kinematic viscosity (m^2 s^{-1})
μ	Dynamic viscosity (kg m^{-1} s^{-1})
σ	Electrically conductivity (S m^{-1})

✉ Shiva Rao
shivarao374@gmail.com

P.N. Deka
pndeka@dibru.ac.in

[1] Department of Mathematics, Dibrugarh University, Dibrugarh 786004, India

ρ Density (kg m^{-3})
κ Thermal conductivity of the nanofluid
γ Chemical reaction parameter
ϕ_1 Volume fraction of Cu nanoparticle
ϕ_2 Volume fraction of Al_2O_3 nanoparticle
Ω Microorganism concentration difference parameter
σ^* Stefan-Boltzmann coefficient
η Similarity variable
ψ Stream function
f' Dimensionless velocity
θ Dimensional temperature
ϕ Dimensionless concentration of nanoparticles
χ Dimensionless concentration of microorganism

Superscript
$'$ Derivative with respect to η

Subscript
w At wall
∞ At free stream region
hnf For hybrid nanofluid
nf For nanofluid with single nanoparticle
f For base fluid
s_1 For Cu nanoparticle
s_2 For Al_2O_3 nanoparticle

1 Introduction

A nanofluid is a type of fluid that consists of suspended nanoparticles, typically ranging in size from 1 to 100 nm. These nanoparticles are often made up of materials such as metals, metal oxides, and carbon-based materials. The unique properties of nanofluids make them a promising field of study for various applications in engineering, such as thermal management, energy conversion, and biomedical applications. One of the most significant advantages of nanofluids over traditional fluids is their superior heat transfer properties. The nanoparticles present in nanofluids increase the surface area, which in turn enhances the thermal conductivity of the fluid. The potential applications of nanofluids include heat exchangers, cooling systems, and electronic devices. However, there are still challenges to be addressed, such as nanoparticle agglomeration and maintaining stable suspensions.

Choi and Eastman were the first to observe that the addition of nanoparticles to base fluid could enhance its thermal conductivity, leading to improved heat transfer rates [1]. Following their discovery, Lee et al. studied the thermal conductivity of various metal oxides and found that both shape and size contribute significantly to the better thermal conductivity of the nanofluid [2]. Buongiorno carried out a study on the factors affecting the thermal conductivity of nanofluids and found that the thermal conductivity could be enhanced by Brownian motion and the thermophoresis effect [3]. Nield and Kuznetsov later utilized Buongiorno's model to analyze the impact of thermal conductivity on the boundary layer stream [4]. Khan and Pop [5] explored the steady flow of nanofluid on a stretching sheet and later Makinde and Aziz [6] investigated the heat transfer characteristics of nanofluid flow using convective boundary conditions.

Boundary-layer theory for a stretched plane has garnered significant interest from researchers and industry experts in view its extensive applications in industry and nanotechnology. Numerous studies have been conducted to investigate various aspects of this theory, including the effects of radiation, heat transfer phenomena, and nanofluid flow problems. One such study conducted by Ishak [7] who focused on the effect of radiation on the boundary layer MHD flow of over an exponentially stretching sheet. Similarly, Hayat et al. [8] explored the heat transfer phenomena of the boundary layer flow over a porous stretching sheet under slip condition. In another study, Muntazir et al. [9] investigated unsteady MHD nanofluid flow problems around a permeable linearly stretched sheet, considering the impact of heat radiation and viscous dissipation. Furthermore, Rao and Deka conducted several numerical investigations on MHD steady and unsteady flows [10, 11] and their possible impacts on thermal radiation and chemical reactions of Casson nanofluid caused due to a stretching sheet. Additionally, Rao and Deka [12] recently conducted a numerical investigation on the effects of solar radiation on heat and mass transfer phenomena of nanofluids. In another study, Alrihieli et al. [13] carried out an investigation on a non-Newtonian nanofluid flow and heat mass transfer in a two-dimensional steady laminar boundary layer caused by a horizontally stretching sheet. The study included heat generation/absorption near a stagnation point and on the radially stretching plate. Very recently, Jawwad et al. [14] examined the MHD boundary layer flow of the Carreau nanofluid, specifically looking at the impact of heat generation/absorption near the stagnation point. Majeed et al. [15] made an investigation which focuses on numerical investigations of the impact of double stratification on radiative mixed convective nanofluid flow over a cylinder. Overall, these studies have contributed significantly to our understanding of boundary-layer theory for a stretched plane and have important implications for industrial and nanotechnological related applications. Some recent studies on boundary layer problem of nanofluids are mention in ref. [16–21].

Hybrid nanofluids are a new type of fluid that combines two or more different nanoparticles dispersed in a base fluid, offering improved thermophysical properties compared to single-component nanofluids. By choosing different types of nanoparticles with varying sizes, shapes, and materials, hybrid nanofluids can be customized for specific applications. For instance, combining nanoparticles with high thermal conductivity and high specific surface area can enhance

the thermal conductivity of the fluid. Similarly, combining nanoparticles with different shapes and sizes can improve the mechanical properties by reducing aggregation and increasing stability. These fluids have been studied for a wide range of applications such as cooling systems in electronic devices, heat transfer fluids in solar collectors, and lubricants in mechanical systems. However, their use in large-scale industrial purpose is still left to be investigated, and more research is needed to understand their properties and optimize their performance. Several studies have been conducted to explore the potential of hybrid nanofluids. Suresh et al. [22] investigated the effect of Al_2O_3-Cu/water hybrid nanofluid in heat transfer. The results indicate possession of higher heat transfer coefficient for hybrid nanofluid other than the base fluid, so the hybrid nanofluid could enhance the heat transfer performance. Hayat and Nadeem [23] conducted a similar study using $Ag-CuO$/water hybrid nanofluid and found that it also improved the heat transfer performance. Sundar et al. [24] provided a comprehensive review of the preparation, thermal properties, heat transfer, and friction factor of hybrid nanofluids. Sarkar et al. [25] conducted a review of recent research on hybrid nanofluids, which showed that these fluids were used in various applications, such as refrigeration, heat exchangers, and solar systems. Muneeshwaran et al. [26] also conducted a review of the role of hybrid nanofluids in heat transfer enhancement and highlighted the potential applications of these fluids in various fields, including electronics cooling, solar thermal energy, and biomedical engineering. The use of hybrid nanofluids in solar systems was also investigated by Shoeibi et al. [27] and Sheikholeslami [28]. In the study carried out by Kursus et al. [29] provided a comprehensive review of the recent progress in the application of nanofluids and hybrid nanofluids in machining. Dinarvand et al. [30] investigated the flow of a blood-based hybrid nanofluid through a converging/diverging channel with multiple slips effect and found that the hybrid nanofluid could improve the flow efficiency. Ullah et al. [31] conducted a numerical analysis of the hybrid nanofluid ($Ag + TiO_2 +$ water) flow in the presence of heat and radiation fluxes and found that the hybrid nanofluid could enhance the heat transfer performance.

While hybrid nanofluids have shown great promise for enhancing heat transfer and thermal conductivity, their stability remains a major challenge. To meet such challenges, attempts are made to introduce microorganism such as bacteria and algae into hybrid nanofluid. The collective motion of these microorganisms creates a density gradient that generates macroscopic convective motion in the fluid, which can increase the stability of the nanofluid. This phenomenon, known as bioconvection, has been extensively studied in recent years for its potential applications in biotechnology, biomicrosystems, and biological systems. Numerous studies have been conducted to investigate different aspects of bioconvection. For instance, Kuznetsov [32] used gyrotactic microorganisms to examine the boundary layer flow of a nanofluid down a horizontal surface. Safdar et al. [33] present a mathematical model to study steady MHD Maxwell nanofluid flow over a porous stretching sheet with gyrotactic microorganisms and reveal that increasing the bioconvection parameter and Peclet number leads to a reduction in the microorganism field. Safdar et al. [34] investigate incompressible, steady, and MHD flow of Buongiorno nanofluid over a stretchable surface. Later Jawad et al. [35] present a mathematical model for evaluating MHD Maxwell nanofluid with heat and mass transfer over a porous stretched sheet, incorporating bioconvection. Khan and Makinde [36] carried out a numerical investigation on the heat and mass transfer phenomena of an MHD nanofluid containing gyrotactic microorganisms along a convectively heated stretching sheet. Furthermore, Khashi'ie et al. [37] numerically examined the effect of using gyrotactic microorganisms in the mixed convection of hybrid nanofluid towards a vertical plate. Shamshuddin et al. [38] investigated how magnetism affects the flow of bioconvection nanofluid across porous media while being influenced by heat radiation caused by stretched surfaces. Finally, Jawad [39] made a numerical investigation of MHD Williamson nanofluid with bioconvection offer valuable insights into its behavior and potential applications in diverse fields, enriching the understanding of nanomaterials in advanced technologies. These studies highlighted the diverse range of applications and potential for bioconvection research.

This study aims to address the gap in the literature by investigating the heat and mass transfer characteristics of bioconvective MHD flow of hybrid nanofluid with motile microorganisms, induced by a permeable stretching sheet in the presence of thermal radiation and chemical reaction. While hybrid nanofluids have been extensively studied for their potential in enhancing heat transfer rates and increasing thermal conductivity, the scope of their use in large-scale industrial applications is still being investigated. One of the major challenges in using these fluids is the issue of stability, which has been addressed by introducing microorganisms such as bacteria and algae. Bioconvection, the collective motion of these microorganisms, has been studied for its potential applications in biotechnology, biomicrosystems, and biological systems. However, there is still a lack of understanding of the heat and mass transfer characteristics of bioconvective MHD flow of hybrid nanofluid with motile microorganisms, and this study may help in the process. This research is important because it could lead to the development of more efficient heat exchangers and other industrial applications. However, the complex nature of these fluids makes it difficult to accurately predict their behavior, and hence, further investigation is required. Our study also investigates the effects of viscous dissipation, Joule heating, and heat generation on the flow. These effects can significantly affect the fluid motion and heat transfer rates,

and therefore, must be taken into account when studying the behavior of these fluids. To investigate the thermal properties of the fluid, we initially suspended the Cu nanoparticles of volume fraction ($\phi_1 = 0.1$) on the base fluid to form the Cu/water nanofluid. Again, to enhance the properties of the fluid, Al_2O_3 nanoparticles of volume fraction ($\phi_2 = 0.1$) are added to the Cu/water nanofluid to form $Cu - Al_2O_3$/water hybrid nanofluid. This hybrid nanofluid has better thermal conductivity than either of its constituents, making it an ideal candidate for heat transfer applications. By using a similarity transformation, we have transformed the governing partial differential equations into ordinary differential equations, which are then solved numerically using an implicit finite difference method known as the Keller-box method. This method is particularly well-suited for solving problems involving fluid flow and heat transfer, and has been used successfully in earlier investigations. Additionally, we calculated the physical quantities that measure the drag force, heat transfer rate, and mass accumulation rate at the surface of the stretching sheet. These quantities provide valuable insights into the behavior of the fluid and can be used to design for optimal performance in the industrial processes that use these fluids.

2 Mathematical Formulation

We consider the steady two-dimensional bioconvective boundary layer flow of an electrically conducting water-based hybrid nanofluid containing motile microorganism over a permeable stretching sheet. The sheet stretching velocity is $u_w(x) = ax$, where a is constant. The coordinate system (x, y) is chosen such that the x-axis is measured along the stretching surface in the direction of the motion and the y-axis is perpendicular to it. A uniform transverse magnetic field of strength B_o is applied parallel to the y-axis. It is also assumed that the surface is maintained at velocity, temperature, concentration, and microorganisms u_w, T_w, C_w, and N_w, respectively, and the same quantities at the boundary layer region are u_∞, T_∞, C_∞, and N_∞ respectively. Schematic diagram of the physical model is shown in Fig. 1.

The aforementioned assumptions and standard boundary conditions are incorporated in the following equations, which describe the MHD bioconvective hybrid nanofluid flow along with heat transfer and mass transfer.

$$\frac{\partial u}{\partial x} + \frac{\partial v}{\partial y} = 0, \tag{1}$$

$$\rho_{hnf}\left(u\frac{\partial u}{\partial x} + v\frac{\partial u}{\partial y}\right) = \mu_{hnf}\,\frac{\partial^2 u}{\partial y^2} - \sigma_{hnf}B_o^2 u - \mu_{hnf}\frac{u}{k_o}, \tag{2}$$

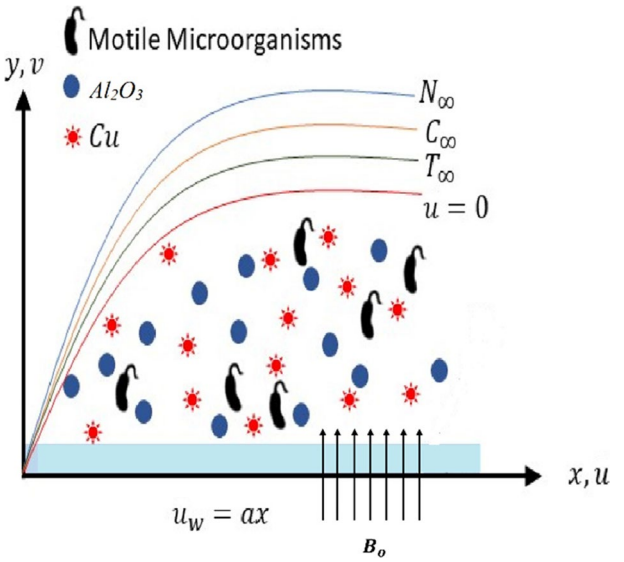

Fig. 1 Schematic diagram of the problem

$$u\frac{\partial T}{\partial x} + v\frac{\partial T}{\partial y} = \frac{\kappa_{hnf}}{(\rho C_p)_{hnf}}\frac{\partial^2 T}{\partial y^2} + \frac{\mu_{hnf}}{(\rho C_p)_{hnf}}\left(\frac{\partial u}{\partial y}\right)^2 + \frac{\sigma_{hnf}}{(\rho C_p)_{hnf}}B_o^2 u^2 + \frac{Q_o}{(\rho C_p)_{hnf}}(T - T_\infty) - \frac{1}{(\rho C_p)_{hnf}}\frac{\partial q_r}{\partial y}, \tag{3}$$

$$u\frac{\partial C}{\partial x} + v\frac{\partial C}{\partial y} = D_m\frac{\partial^2 C}{\partial y^2} - Kr\left(C - C_\infty\right), \tag{4}$$

$$u\frac{\partial N}{\partial x} + v\frac{\partial N}{\partial y} = D_n\frac{\partial^2 N}{\partial y^2} - \left(\frac{bW_c}{C - C_\infty}\right)\frac{\partial}{\partial y}\left(N\frac{\partial C}{\partial y}\right). \tag{5}$$

The following are the initial and boundary conditions:

$$\begin{aligned} &u = u_w(x) = ax, \quad v = 0,\ T = T_w,\ C = C_w,\ N = N_w, \quad when\ y = 0,\\ &u \to 0, \qquad\qquad T \to T_\infty,\ C \to C_\infty,\ N \to N_\infty,\ as\ y \to \infty \end{aligned} \tag{6}$$

The Rosseland approximation for radiative heat flux can be mathematically written as [40–42]:

$$\frac{\partial q_r}{\partial y} = \frac{-4\sigma^*}{3k^*}\frac{\partial T^4}{\partial y}, \tag{7}$$

By generalizing the Taylor series and ignoring the higher order terms, we are able to get:

$$T^4 = 4\,T_\infty^3\,T - 3\,T_\infty^4,$$

Hence, Eq. (7) becomes:

$$\frac{\partial q_r}{\partial y} = \frac{-16\sigma^*}{3k^*}\,T_\infty^3\frac{\partial^2 T}{\partial y^2}, \tag{8}$$

We use the similarity transformation [43]:

$$\eta=\sqrt{\frac{a}{\nu_f}}y,\ \psi=\sqrt{a\nu_f}xf(\eta),\ \theta(\eta)=\frac{T-T_\infty}{T_w-T_\infty},\ \phi(\eta)=\frac{C-C_\infty}{C_w-C_\infty},\ \chi(\eta)=\frac{N-N_\infty}{N_w-N_\infty},\ u=\frac{\partial\psi}{\partial y}=axf'(\eta)\ \ and\ \ v=-\frac{\partial\psi}{\partial x}=-\sqrt{a\nu_f}f(\eta). \tag{9}$$

The thermo-physical attributes are given in Tables 1 and 2. Substituting (9) in Eqs. (1) to (5), we get:

$$f'''+\frac{A_2}{A_1}ff''-\frac{A_2}{A_1}f'^2-\left(\frac{A_5M}{A_1}+K_p\right)f'=0, \tag{10}$$

$$\frac{\theta''}{\Pr}\left(A_4+\frac{4}{3}Rd\right)+A_3f\theta'+A_1Ecf''^2+A_5MEcf'^2+Q\theta=0, \tag{11}$$

$$\frac{\phi''}{Sc}+f\phi'-\gamma\phi=0, \tag{12}$$

$$\chi''+Sbf\chi'-Pe\left[\phi'\chi'+(\Omega+\chi)\phi''\right]=0 \tag{13}$$

The boundary condition (6) is transformed to:

$$f(0)=0,\quad f'(0)=1,\quad \theta(0)=1,\quad \phi(0)=1,\quad \chi(0)=1,\quad f'(\infty)\to 0,\quad \theta(\infty)\to 0,\quad \phi(\infty)\to 0,\quad \chi(\infty)\to 0. \tag{14}$$

Here $A_i(i=1,2,3,4,5)$ are defined in the following ways:

$$A_1=\frac{\mu_{hnf}}{\mu_f},\qquad A_2=\frac{\rho_{hnf}}{\rho_f},\qquad A_3=\frac{(\rho C_p)_{hnf}}{(\rho C_p)_f},$$
$$A_4=\frac{\kappa_{hnf}}{\kappa_f},\qquad A_5=\frac{\sigma_{hnf}}{\sigma_f},$$

In this study, we specify the flow parameters as follows:

$$M=\frac{\sigma_f B_o^2}{a\rho_f},\quad K_p=\frac{\nu_f}{ak_o},\quad \Pr=\frac{\nu_f(\rho C_p)_f}{\kappa_f},\quad Rd=\frac{4\sigma^*T_\infty^3}{k^*\kappa_f},$$

$$Ec=\frac{(ax)^2\rho_f}{(\rho C_p)_f(T_w-T_\infty)},\quad Q=\frac{Q_o}{a(\rho C_p)_f},\quad Sc=\frac{\nu_f}{D_m},$$

Table 1 Thermophysical properties of water and nanoparticles

	ρ (kg/m^3)	κ (W/mK)	σ (S/m)	C_p(J/kgK)
H_20	997.1	0.613	5.5×10^{-6}	4179
Cu	8933	401	59.6×10^{6}	385
Al_2O_3	3970	40	35×10^{6}	765

$$\gamma=\frac{Kr}{a},\ Sb=\frac{\nu}{Dn},\ Pe=\frac{bWc}{D_n},\ \Omega=\frac{N_\infty}{N_w-N_\infty}.$$

The shear stress is defined as:

$$\tau_w=\left[\mu_f\frac{\partial u}{\partial y}\right]_{y=0}=\mu ax\sqrt{\frac{a}{\nu_f}}f''(0),$$

The local surface heat flux and local mass flux is defined as:

$$q_w=-\left(\kappa_f+\frac{16\sigma^*T_\infty^3}{3k^*}\right)\left[\frac{\partial T}{\partial y}\right]_{y=0}=-\kappa_f\left(1+\frac{4}{3}Rd\right)(T_w-T_\infty)\sqrt{\frac{a}{\nu_f}}\theta'(0),$$

$$q_m=-D_m\left[\frac{\partial C}{\partial y}\right]_{y=0}=-D_m(C_w-C_\infty)\sqrt{\frac{a}{\nu_f}}\phi'(0),$$

$$q_n=-D_m\left[\frac{\partial N}{\partial y}\right]_{y=0}=-D_n(C_w-C_\infty)\sqrt{\frac{a}{\nu_f}}\chi'(0),$$

The bodily measure is the local surface drag Cf_x, thermal gradient Nu_x, mass gradient Sh_x, and motile microorganism flux Nn_x and is given as:

Table 2 Thermophysical properties model for hybrid nanofluid

Property	Hybrid nanofluid
Density	$\rho_{hnf}=(1-\phi_2)[(1-\phi_1)\rho_f+\phi_1\rho_{s1}]+\phi_2\rho_{s2}$
Dynamic viscosity	$\mu_{hnf}=\frac{\mu_f}{(1-\phi_1)^{2.5}(1-\phi_2)^{2.5}}$
Heat capacity	$(\rho C_p)_{hnf}=(1-\phi_2)[(1-\phi_1)(\rho C_p)_f+\phi_1(\rho C_p)_{s1}]+\phi_2(\rho C_p)_{s2}$
Thermal conductivity	$\kappa_{hnf}=\frac{\kappa_{s2}+2\kappa_{nf}-2\phi_2(\kappa_{nf}-\kappa_{s2})}{\kappa_{s2}+2\kappa_{nf}+\phi_2(\kappa_{nf}-\kappa_{s2})}\times\kappa_{nf}$ where, $\kappa_{nf}=\frac{\kappa_{s1}+2\kappa_f-2\phi_1(\kappa_f-\kappa_{s1})}{\kappa_{s1}+2\kappa_f+\phi_1(\kappa_f-\kappa_{s1})}\times\kappa_f$
Electrical conductivity	$\sigma_{hnf}=\left[1+\frac{3\left(\frac{\sigma_{s2}}{\sigma_{nf}}-1\right)\phi_2}{\left(\frac{\sigma_{s2}}{\sigma_{nf}}+2\right)-\left(\frac{\sigma_{s2}}{\sigma_{nf}}-1\right)\phi_2}\right]\times\sigma_{nf}$ where, $\sigma_{nf}=\left[1+\frac{3\left(\frac{\sigma_{s1}}{\sigma_f}-1\right)\phi_1}{\left(\frac{\sigma_{s1}}{\sigma_f}+2\right)-\left(\frac{\sigma_{s1}}{\sigma_f}-1\right)\phi_1}\right]\times\sigma_f$

$$Cf_x = \frac{\tau_w}{\rho_f u^2} = \frac{f''(0)}{x}\sqrt{\frac{\nu_f}{a}},\quad Nu_x = \frac{xq_w}{\kappa_f\left(T_w - T_\infty\right)},$$
$$Sh_x = \frac{xq_m}{D_m\left(C_w - C_\infty\right)},\quad Nn_x = \frac{xq_n}{D_n\left(N_w - N_\infty\right)}.$$

Hence,

$$\sqrt{Re_x}Cf_x = f''(0),$$

$$\frac{Nu_x}{\sqrt{Re_x}} = -\left(1 + \frac{4}{3}Rd\right)\theta'(0),$$

$$\frac{Sh_x}{\sqrt{Re_x}} = -\phi'(0),$$

$$\frac{Nn_x}{\sqrt{Re_x}} = -\chi'(0),$$

where $Re_x = \frac{xu_w}{\nu_f}$ stands for local Reynolds number.

3 Method of Solution

The Keller-box technique is a powerful numerical method used for solving a system of equations that describe a non-linear problem, namely Eqs. (10) to (13) with boundary condition given by equation (14). This method is chosen for its flexibility and remarkable accuracy, having demonstrated an error of order 10^{-5} in solving similar problems. The technique is implemented here using the methodology developed by Cebeci and Bradshaw [44].

The computational steps involved in the Keller-box technique are as follows.

a. To reduce the obtained ordinary differential equations (ODE) into the system of first-order equations.
b. To write the reduced equations in finite difference.
c. To linearize the equations using Newton method and writing them in vector form.
d. To solve the linear equations which involve the tri-diagonal matrix.

In order to solve the obtained non-linear ODE's, Eqs. (10) to (13) along with the boundary condition (14) are transformed into the system of first-order equations and then are expressed in finite difference using central differences. So, we introduce some new dependent variable $p(\eta)$, $q(\eta)$, $t(\eta)$, $v(\eta)$, $x(\eta)$ as:

$$f' = p,\ p' = q,\ \theta' = t,\ \phi' = v,\ \chi' = x \tag{15}$$

where prime ($'$) represents the differentiation with respect to η.

Equations (10) to (13) can now be written as:

$$q' + \frac{A_2}{A_1}fq - \frac{A_2}{A_1}p^2 - \left(\frac{A_5}{A_1}M + K_p\right)p = 0, \tag{16}$$

$$\frac{1}{\Pr}\left(A_4 + \frac{4}{3}Rd\right)t' + A_3 ft + A_1 Ec\left(q^2\right) + MEc\left(p^2\right) + Q\theta = 0, \tag{17}$$

$$v' + Sb(fv) - \gamma\ Sb\ \phi = 0 \tag{18}$$

$$x' + Sbfx - Pe\left[vx + (\Omega + \chi)v'\right] = 0. \tag{19}$$

The boundary condition (14) can be written as:

$$f(0) = 0,\ p(0) = 1,\ \theta(0) = 1,\ \phi(0) = 1,\ \chi(0) = 1,$$

$$p(\eta) \to 0,\ \theta(\eta) \to 0\ \phi(\eta) \to 0,\ \chi(\eta) \to 0\ as\ \eta \to 0. \tag{20}$$

Next, we consider a segment $[\eta_{j-1}, \eta_j]$ with $\eta_{j-1/2}$ as its midpoint, which is defined below:

$$\eta_0 = 0,\ \eta_j = \eta_{j-1} + h_j,\ \eta_J = \eta_\infty \tag{21}$$

Let us assume that $\Delta\eta_j$ where $j = 1, 2, \ldots, J$ indicates the coordinate location and h_j is the $\Delta\eta_j$-spacing. For the midpoints $\eta_{j-1/2}$, we have written a set of approximations (16) to (19) in terms of finite differences.

$$f_j - f_{j-1} - \frac{1}{2}h_j\left(p_j + p_{j-1}\right) = 0, \tag{22}$$

$$p_j - p_{j-1} - \frac{1}{2}h_j\left(q_j + q_{j-1}\right) = 0, \tag{23}$$

$$\theta_j - \theta_{j-1} - \frac{1}{2}h_j\left(t_j + t_{j-1}\right) = 0, \tag{24}$$

$$\phi_j - \phi_{j-1} - \frac{1}{2}h_j\left(v_j + v_{j-1}\right) = 0, \tag{25}$$

$$\chi_j - \chi_{j-1} - \frac{1}{2}h_j\left(x_j + x_{j-1}\right) = 0, \tag{26}$$

$$q_j - q_{j-1} + h_j\frac{A_2}{A_1}(fq)_{j-1/2} - h_j\frac{A_2}{A_1}p^2_{j-1/2} - h_j\left(\frac{A_5}{A_1}M + K_p\right)p_{j-1/2} = 0, \tag{27}$$

$$\frac{1}{\Pr}\left(A_4 + \frac{4}{3}Rd\right)(t_j - t_{j-1}) + h_j A_3(ft)_{j-1/2} + h_j A_1 Ec\, q^2_{j-1/2} + h_j Q\theta_{j-1/2} + h_j A_5 M\, Ec\, p^2_{j-1/2} = 0, \tag{28}$$

$$v_j - v_{j-1} + h_j Sb(fv)_{j-1/2} - h_j \gamma Sb\ \phi_{j-1/2} = 0, \tag{29}$$

$$x_j - x_{j-1} + h_j Sb(fx)_{j-1/2} - Pe\left[h_j(vx)_{j-1/2} + \left(\Omega + \chi_{j-1/2}\right)\left(v_j - v_{j-1}\right)\right]. \tag{30}$$

where $j = 1, 2, 3, \ldots, J$ and η_J is sufficiently large so that it is beyond region of the boundary layer.

The boundary conditions (20) become:

$$f_o = 0,\ p_o = 1,\ \theta_o = 1,\ \phi_o = 1,\ \chi_o = 1$$

$$p_J = 0,\ \theta_J = 0,\ \phi_J = 0,\ \chi_J = 0 \tag{31}$$

We utilize Newton's method to linearize the non-linear system of equations by applying the following equations:

$$\begin{aligned} f_j^{(k+1)} &= f_j^{(k)} + \delta f_j^{(k)},\ p_j^{(k+1)} = p_j^{(k)} + \delta p_j^{(k)},\ q_j^{(k+1)} \\ &= q_j^{(k)} + \delta q_j^{(k)},\ \theta_j^{(k+1)} = \theta_j^{(k)} + \delta\theta_j^{(k)},\ t_j^{(k+1)} \\ &= t_j^{(k)} + \delta t_j^{(k)},\ \phi_j^{(k+1)} = \phi_j^{(k)} + \delta\phi_j^{(k)},\ v_j^{(k+1)} \\ &= v_j^{(k)} + \delta v_j^{(k)},\ \chi_j^{(k+1)} = \chi_j^{(k)} + \delta\chi_j^{(k)} \\ x_j^{(k+1)} &= x_j^{(k)} + \delta x_j^{(k)} \end{aligned} \tag{32}$$

where $k = 0, 1, 2, 3, \ldots$.

Taking k out of the equations the sake of simplicity, Eqs. (22) to (30) may now be stated linearly as:

$$\delta f_i - \delta f_{i-1} - \frac{h_j}{2}\left(\delta p_j + \delta p_{j-1}\right) = \left(r_1\right)_{j-1/2}, \tag{33}$$

$$\delta p_j - \delta p_{j-1} - \frac{h_j}{2}\left(\delta q_j + \delta q_{j-1}\right) = \left(r_2\right)_{j-1/2}, \tag{34}$$

$$\delta\theta_j - \delta\theta_{j-1} - \frac{h_j}{2}\left(\delta t_j + \delta t_{j-1}\right) = \left(r_3\right)_{j-1/2}, \tag{35}$$

$$\delta\phi_j - \delta\phi_{j-1} - \frac{h_j}{2}\left(\delta v_j + \delta v_{j-1}\right) = \left(r_4\right)_{j-1/2}, \tag{36}$$

$$\delta\chi_j - \delta\chi_{j-1} - \frac{h_j}{2}\left(\delta x_j + \delta x_{j-1}\right) = \left(r_5\right)_{j-1/2}, \tag{37}$$

$$\begin{aligned} &\left(a_1\right)\delta q_j + \left(a_2\right)\delta q_{j-1} + \left(a_3\right)\delta f_j + \left(a_4\right)\delta f_{j-1} \\ &\quad + \left(a_5\right)\delta p_j + \left(a_6\right)\delta p_{j-1} = \left(r_6\right)_{j-1/2}, \end{aligned} \tag{38}$$

$$\begin{aligned} &\left(b_1\right)\delta t_j + \left(b_2\right)\delta t_{j-1} + \left(b_3\right)\delta f_j + \left(b_4\right)\delta f_{j-1} + \left(b_5\right)\delta q_j + \left(b_6\right)\delta q_{j-1} \\ &\quad + \left(b_7\right)\delta p_j + \left(b_8\right)\delta p_{j-1} + \left(b_9\right)\delta\theta_j + \left(b_{10}\right)\delta\theta_{j-1} = \left(r_7\right)_{j-1/2}, \end{aligned} \tag{39}$$

$$\begin{aligned} &\left(c_1\right)\delta v_j + \left(c_2\right)\delta v_{j-1} + \left(c_3\right)\delta f_j + \left(c_4\right)\delta f_{j-1} \\ &\quad + \left(c_5\right)\delta\phi_j + \left(c_6\right)\delta\phi_{j-1} = \left(r_8\right)_{j-1/2}, \end{aligned} \tag{40}$$

$$\begin{aligned} &\left(d_1\right)\delta x_j + \left(d_2\right)\delta x_{j-1} + \left(d_3\right)\delta f_j + \left(d_4\right)\delta f_{j-1} \\ &\quad + \left(d_5\right)\delta v_j + \left(d_6\right)\delta v_{j-1} = \left(r_9\right)_{j-1/2}. \end{aligned} \tag{41}$$

where,

$$\left(a_1\right) = 1 + \frac{h_j}{2}\frac{A_2}{A_1}f_{j-1/2},$$

$$\left(a_2\right)_j = \left(a_1\right)_j - 2,$$

$$\left(a_3\right)_j = \frac{h_j}{2}\frac{A_2}{A_1}q_{j-1/2},$$

$$\left(a_4\right)_j = \left(a_3\right)_j,$$

$$\left(a_5\right)_j = -\frac{h_j}{2}\frac{A_2}{A_1}p_{j-1/2} - \frac{h_j}{2}\left(\frac{A_5}{A_1}M + K_P\right),$$

$$\left(a_6\right)_j = \left(a_5\right)_j,$$

$$\left(b_1\right)_j = \frac{1}{\mathrm{Pr}}\left(A_4 + \frac{4}{3}Rd\right) + \frac{h_j}{2}A_3 f_{j-1/2},$$

$$\left(b_2\right)_j = \left(b_1\right)_j - \frac{2}{\mathrm{Pr}}\left(A_4 + \frac{4}{3}Rd\right),$$

$$\left(b_3\right)_j = \frac{h_j}{2}A_3 t_{j-1/2},$$

$$\left(b_4\right)_j = \left(b_3\right)_j,$$

$$\left(b_5\right)_j = \frac{h_j}{2}A_1 Ec\ q_{j-1/2},$$

$$\left(b_6\right)_j = \left(b_5\right)_j,$$

$$\left(b_7\right)_j = \frac{h_j}{2}A_5 Ec\ Mp_{j-1/2},$$

$$\left(b_8\right)_j = \left(b_7\right)_j,$$

$$\left(b_9\right)_j = \frac{h_j}{2}Q,$$

$$(b_{10})_j = (b_9)_j,$$

$$(c_1)_j = 1 + \frac{h_j}{2} Le\, f_{j-1/2},$$

$$(c_2)_j = (c_1)_j - 2,$$

$$(c_3)_j = \frac{h_j}{2} Sb\, v_{j-1/2},$$

$$(c_4)_j = (c_3)_j,$$

$$(c_5)_j = -\gamma \frac{h_j}{2} Sb,$$

$$(r_5) = \chi_{j-1} - \chi_j + h_j (v_{j-1/2}),$$

$$(r_6) = q_{j-1} - q_j - h_j \frac{A_2}{A_1} (fq)_{j-1/2} + h_j \frac{A_2}{A_1} p^2_{j-1/2} + h_j \left(\frac{A_5}{A_1} M + K_p \right) p_{j-1/2},$$

$$(r_7) = \frac{1}{\Pr} \left(A_4 + \frac{4}{3} Rd \right) (t_{j-1} - t_j) - h_j A_3 (ft)_{j-1/2} - h_j A_1 Ec\, q^2_{j-1/2} - h_j Q \theta_{j-1/2} - h_j A_5 M\, Ec\, p^2_{j-1/2},$$

$$(r_8) = v_{j-1} - v_j - h_j Sb (fv)_{j-1/2} + h_j \gamma Sb\, \phi_{j-1/2},$$

$$(r_9) = x_{j-1} - x_j - h_j Sb (fx)_{j-1/2} + Pe \left[h_j (vx)_{j-1/2} + (\Omega + \chi_{j-1/2}) (v_j - v_{j-1}) \right].$$

The boundary condition (1) is reduced to:

$$\delta f_o = 0, \quad \delta p_o = \delta q_o, \quad \delta q_o = \delta t_o, \quad \delta \theta_o = 0, \quad \delta \phi_o = 0, \quad \delta p_J = 0, \quad \delta \theta_J = 0, \quad \delta \phi_J = 0$$

$$(c_6)_j = -(c_5)_j,$$

$$(d_1)_j = 1 + \frac{h_j}{2} Sb\, f_{j-1/2} - \frac{h_j}{2} Pe v_{j-1/2},$$

$$(d_2)_j = (d_1)_j - 2,$$

$$(d_3)_j = \frac{h_j}{2} Sb\, x_{j-1/2},$$

$$(d_4)_j = (d_3)_j,$$

$$(d_5)_j = -Pe \left[\chi_{j-1/2} + \Omega + \frac{h_j}{2} x_{j-1/2} \right],$$

$$(d_6)_j = -(d_5)_j,$$

$$(r_1) = f_{j-1} - f_j + h_j (p_{j-1/2}),$$

$$(r_2) = p_{j-1} - p_j + h_j (q_{j-1/2}),$$

$$(r_3) = \theta_{j-1} - \theta_j + h_j (t_{j-1/2}),$$

$$(r_4) = \phi_{j-1} - \phi_j + h_j (v_{j-1/2}),$$

The linearized difference equation of the system (33)–(41) has a block tridiagonal structure and may thus be solved using the block elimination approach as described by Cebeci and Bradshaw [44]. It may be expressed as in vector matrix form:

$$A\delta = r$$

where,

$$A = \begin{bmatrix} [A_1] & [C_1] & & & & \\ [B_2] & [A_2] & [C_2] & & & \\ & \ddots & \ddots & \ddots & & \\ & & [B_{j-1}] & [A_{j-1}] & [C_{j-1}] & \\ & & & [B_j] & [A_j] \end{bmatrix}, \delta = \begin{bmatrix} [\delta_1] \\ [\delta_2] \\ [\delta_3] \\ \vdots \\ [\delta_{j-1}] \\ [\delta_j] \end{bmatrix} \text{ and } r = \begin{bmatrix} [r_1] \\ [r_2] \\ [r_3] \\ \vdots \\ [r_{j-1}] \\ [r_j] \end{bmatrix}$$

Here,

$$[A_1] = \begin{bmatrix} 0 & 0 & 0 & 0 & 1 & 0 & 0 & 0 & 0 \\ -\frac{h_j}{2} & 0 & 0 & 0 & 0 & -\frac{h_j}{2} & 0 & 0 & 0 \\ 0 & -\frac{h_j}{2} & 0 & 0 & 0 & 0 & -\frac{h_j}{2} & 0 & 0 \\ 0 & 0 & -\frac{h_j}{2} & 0 & 0 & 0 & 0 & -\frac{h_j}{2} & 0 \\ 0 & 0 & 0 & -\frac{h_j}{2} & 0 & 0 & 0 & 0 & -\frac{h_j}{2} \\ (a_2)_J & 0 & 0 & 0 & (a_3)_J & (a_1)_J & 0 & 0 & 0 \\ (b_6)_J & (b_2)_J & 0 & 0 & (b_3)_J & (b_5)_J & (b_1)_J & 0 & 0 \\ 0 & 0 & (c_2)_J & 0 & (c_3)_J & 0 & 0 & (c_1)_J & 0 \\ 0 & 0 & (d_6)_J & (d_2)_J & (d_3)_J & 0 & 0 & (d_5)_J & (d_1)_J \end{bmatrix},$$

For $1 \le j \le J$

$$[A_J]=\begin{bmatrix} -\frac{h_j}{2} & 0 & 0 & 0 & 1 & 0 & 0 & 0 & 0 \\ -1 & 0 & 0 & 0 & 0 & -\frac{h_j}{2} & 0 & 0 & 0 \\ 0 & -1 & 0 & 0 & 0 & 0 & -\frac{h_j}{2} & 0 & 0 \\ 0 & 0 & -1 & 0 & 0 & 0 & 0 & -\frac{h_j}{2} & 0 \\ 0 & 0 & 0 & -1 & 0 & 0 & 0 & 0 & -\frac{h_j}{2} \\ (a_6)_J & 0 & 0 & 0 & (a_3)_J & (a_1)_J & 0 & 0 & 0 \\ (b_8)_J & (b_{10})_J & 0 & 0 & (b_3)_J & (b_5)_J & (b_1)_J & 0 & 0 \\ 0 & 0 & (c_6)_J & 0 & (c_3)_J & 0 & 0 & (c_1)_J & 0 \\ 0 & 0 & 0 & 0 & (d_3)_J & 0 & 0 & (d_5)_J & (d_1)_J \end{bmatrix},$$

$$[B_J]=\begin{bmatrix} 0\,0\,0\,0 & -1 & 0 & 0 & 0 & 0 \\ 0\,0\,0\,0 & 0 & -\frac{h_j}{2} & 0 & 0 & 0 \\ 0\,0\,0\,0 & 0 & 0 & -\frac{h_j}{2} & 0 & 0 \\ 0\,0\,0\,0 & 0 & 0 & 0 & -\frac{h_j}{2} & 0 \\ 0\,0\,0\,0 & 0 & 0 & 0 & 0 & -\frac{h_j}{2} \\ 0\,0\,0\,0 & (a_4)_J & (a_2)_J & 0 & 0 & 0 \\ 0\,0\,0\,0 & (b_4)_J & (b_6)_J & (b_2)_J & 0 & 0 \\ 0\,0\,0\,0 & (c_4)_J & 0 & 0 & (c_2)_J & 0 \\ 0\,0\,0\,0 & (d_4)_J & 0 & 0 & (d_6)_J & (d_2)_J \end{bmatrix},$$

For $2 \le j \le J-1$

$$[C_J]=\begin{bmatrix} -\frac{h_j}{2} & 0 & 0 & 0\,0\,0\,0\,0\,0 \\ 1 & 0 & 0 & 0\,0\,0\,0\,0\,0 \\ 0 & 1 & 0 & 0\,0\,0\,0\,0\,0 \\ 0 & 0 & 1 & 0\,0\,0\,0\,0\,0 \\ 0 & 0 & 0 & 1\,0\,0\,0\,0\,0 \\ (a_5)_J & 0 & 0 & 0\,0\,0\,0\,0\,0 \\ (b_7)_J & (b_9)_J & 0 & 0\,0\,0\,0\,0\,0 \\ 0 & 0 & (c_5)_J & 0\,0\,0\,0\,0\,0 \\ 0 & 0 & 0 & 0\,0\,0\,0\,0\,0 \end{bmatrix},$$

$$[\delta_1]=\begin{bmatrix} \delta q_0 \\ \delta\theta_0 \\ \delta\phi_0 \\ \delta\chi_o \\ \delta f_1 \\ \delta q_1 \\ \delta t_1 \\ \delta v_1 \\ \delta x_1 \end{bmatrix},\ \text{For, } 2 \le j \le J\ \ [\delta_j]=\begin{bmatrix} \delta q_{j-1} \\ \delta\theta_{j-1} \\ \delta\phi_{j-1} \\ \delta\chi_{j-1} \\ \delta f_j \\ \delta q_j \\ \delta t_j \\ \delta v_j \\ \delta x_j \end{bmatrix} \text{ and } 1 \le j \le J\ \ [r_j]=\begin{bmatrix} (r_1)_{j-1/2} \\ (r_2)_{j-1/2} \\ (r_3)_{j-1/2} \\ (r_4)_{j-1/2} \\ (r_5)_{j-1/2} \\ (r_6)_{j-1/2} \\ (r_7)_{j-1/2} \\ (r_7)_{j-1/2} \\ (r_7)_{j-1/2} \end{bmatrix}$$

Assuming $|A| \neq 0$, it can be factorized as $A = LU$. This block tri-diagonal structure can be solved using LU method.

One of the primary aspects influencing the method's accuracy is the initial guesses. They are as follows:

$$f_0(\eta)=e^{-\eta}, \qquad \theta_0(\eta)=e^{-\eta}, \qquad \phi_0(\eta)=e^{-\eta}, \qquad \text{and} \qquad \chi_o(\eta)=e^{-\eta}$$

In this study, uniform grid of size $\Delta\eta_j = 0.006$ is considered, and solutions are produced with an error tolerance of 10^{-5} in all situations, resulting in an accuracy of four decimal places for the majority of the given quantities as indicated in all tables.

4 Results and Discussion

To investigate the physical representation of the problem, the numerical results were presented in both graphical and tabular forms. The velocity, temperature, concentration, and microorganism concentration profiles were plotted on graphs to show the influence of various parameters, while tables were used to display numerical values of skin-friction coefficient, local Nusselt number, local Sherwood number, and local density number of motile microorganisms. The Keller-box method was employed to obtain all the graphs and numerical values by developing a MATLAB code. To ensure the validity of our results, we compared them with those of previous studies conducted by Wang et al. [45], Khan and Pop [5], and Waini et al. [46]. The results presented in Table 3 showed excellent compliance and higher accuracy, which gave us confidence that our analysis was reliable and efficient.

Figures 2, 3, 4, and 5 show how the flow momentum for the microorganism nanofluid flow responds to changes in different parameters. In Fig. 2, the observed variation of velocity follows a reduction pattern as the magnetic parameters (M) increase. The magnetic parameter represents the strength of the applied magnetic field, and its rising values indicate a greater resistive force opposing the fluid flow. This resistive force, known as the Lorentz force, arises from the interaction between the magnetic field and the electrically charged nanoparticles present in the nanofluid. As the magnetic field strength increases (higher M values), the Lorentz force becomes more pronounced, opposing the fluid flow more effectively. Consequently, the fluid experiences a decrease in flow velocity. The resistive Lorentz force acts as a drag force, slowing down the movement of the fluid, particularly near the walls of the flow channel. From Fig. 3, it is found that the increasing porosity parameter (K_p) also leads to the decrease in flow velocity. This is due to the fact that increasing K_p decreases the amount of Darcian body force and thus slows the fluid. Figures 4 and 5 indicate the enhancement in velocity profile with volume fraction of Cu (ϕ_1) and Al_2O_3 (ϕ_2) nanoparticles, respectively. This increase can be attributed to the fact that both copper and alumina are known to have high thermal conductivities, which help to enhance heat transfer rates. This, in turn, leads to an increase in the momentum transfer of the fluid, thereby increasing the velocity profile. Additionally, the presence of copper and alumina nanoparticles in the fluid also leads

Table 3 Comparison for values of $-\theta'(0)$ for ordinary fluid ($\phi_1=0$ and $\phi_2=0$) with various values of Pr when $K=M=K_p=Rd=E_c=Q=0$ and $\lambda=1$

Pr	Wang et al. [45]	Khan and Pop [5]	Waini et al. [46]	Present
2	0.9114	0.9113	0.911353	0.9107
6.13	-	-	1.759682	1.7592
7	1.8954	1.8954	1.895400	1.8949
20	3.3539	3.3539	3.353902	3.3535

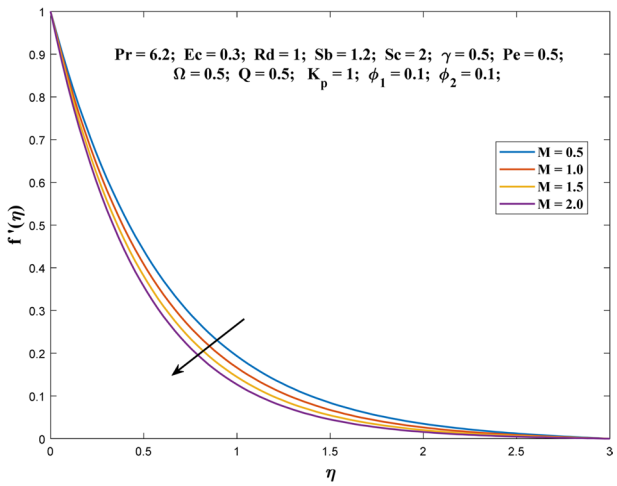

Fig. 2 Variation in $f'(\eta)$ with M

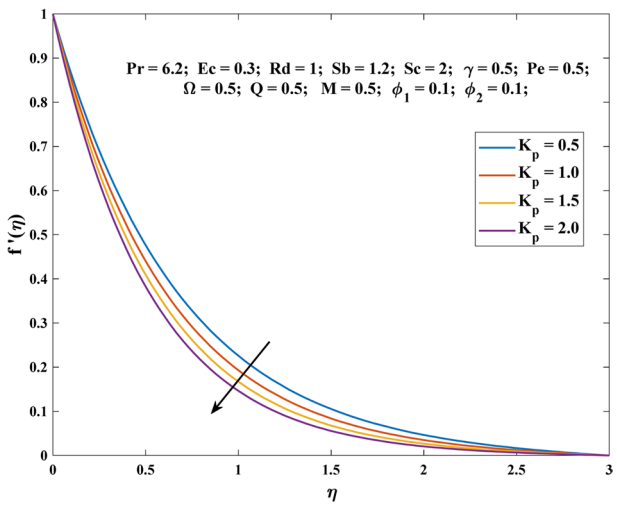

Fig. 3 Variation in $f'(\eta)$ with K_p

to the reduction in the formation of agglomerates that can cause an increase in the fluid viscosity.

Figures 6, 7, 8, and 9 depict the significant influence of magnetic parameter (M), porosity parameter (K_p), Eckert

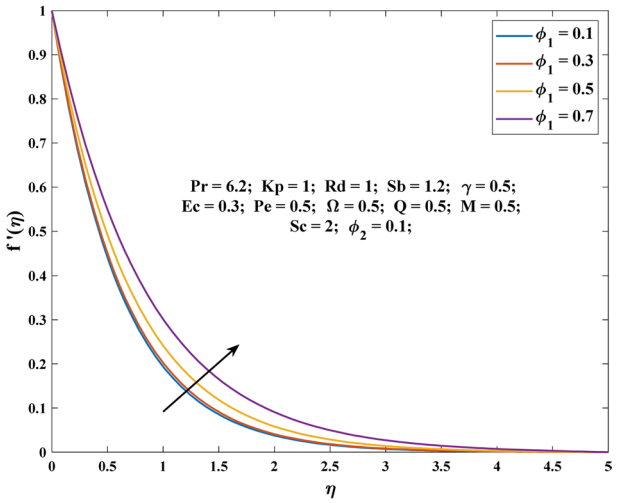

Fig. 4 Variation in $f'(\eta)$ with ϕ_1

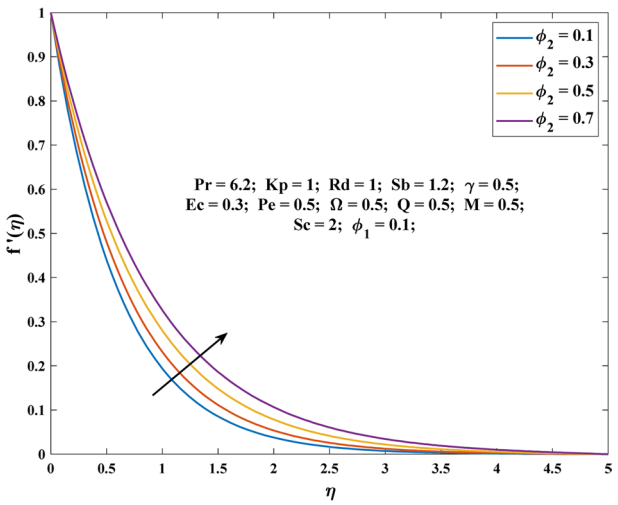

Fig. 5 Variation in $f'(\eta)$ with ϕ_2

number (Ec), and radiation parameter (Rd) on the temperature profile of the nanofluid. In Fig. 6, the enhancement in the temperature profile is directly linked to the magnetic parameter (M). The variation in M generates the Lorentz force, which intensifies friction between fluid layers. As a consequence, the temperature rises within the nanofluid. This physical phenomenon is crucial because it demonstrates the role of M in modifying thermal characteristics, emphasizing the importance of magnetic effects on heat transfer in nanofluids. Moving to Fig. 7, an evident rise in temperature is observed with increasing porosity parameter (K_p). The porosity parameter induces internal heat generation within the nanofluid, thereby elevating the temperature profile. This finding holds significance in practical applications where

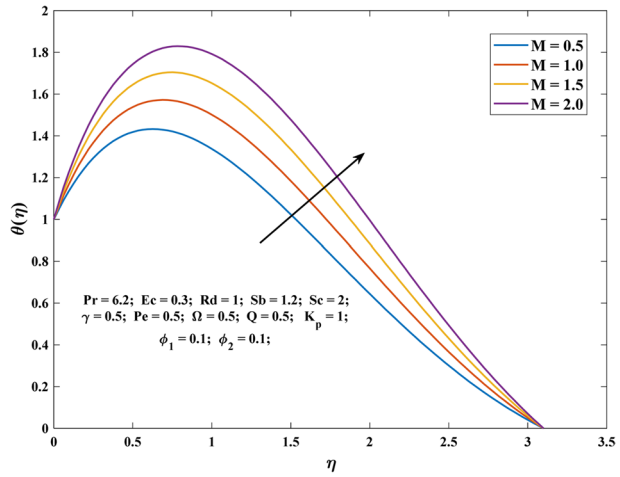

Fig. 6 Variation in $\theta(\eta)$ with M

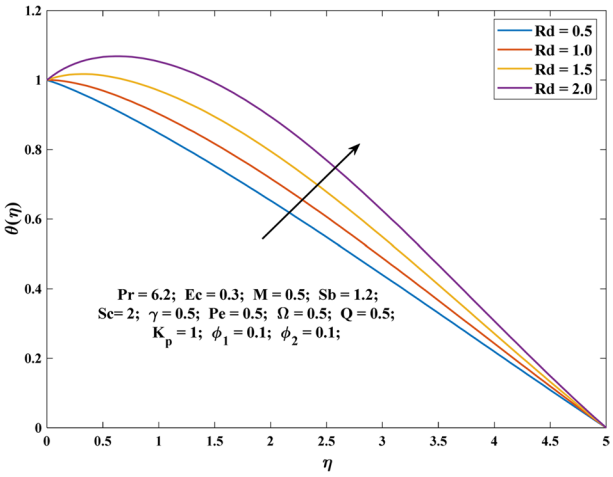

Fig. 9 Variation in $\theta(\eta)$ with Rd

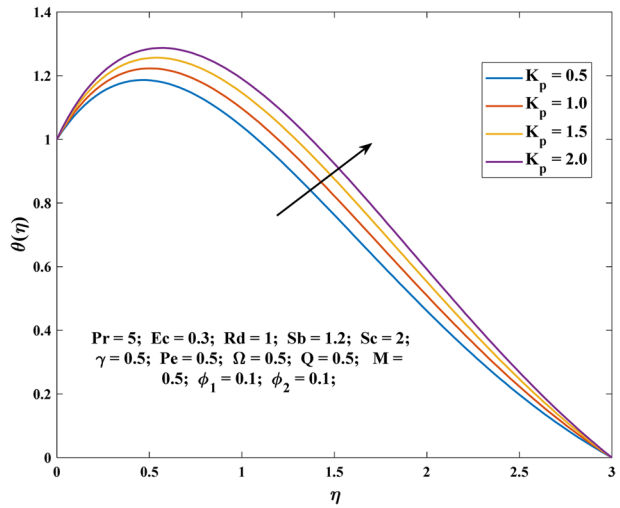

Fig. 7 Variation in $\theta(\eta)$ with K_p

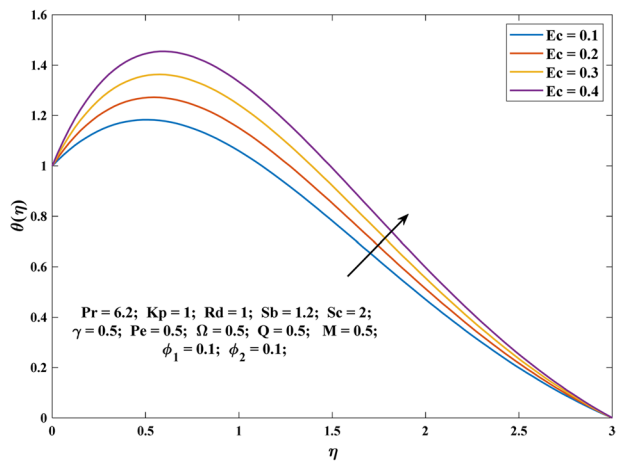

Fig. 8 Variation in $\theta(\eta)$ with Ec

porous media or materials with internal heat sources are involved. It highlights the impact of K_p on heat transfer within the nanofluid, making it a key factor to consider in designing efficient heat exchange systems. Figure 8 reveals an upsurge in the temperature profile with an increase in the Eckert number (Ec). Physically, this temperature rise is attributed to the production of frictional energy caused by the collision of fluid particles. Finally, Fig. 9 demonstrates how the temperature profile increases with a higher radiation parameter (Rd). The rise in heat flux at the surface of the nanofluid is responsible for this effect. The increase in Rd intensifies radiative heat transfer, contributing to the overall upsurge in the temperature profile.

The response of mass specie transfer to the rising value of magnetic parameter, chemical reaction parameter, and Schmidt number is investigated in Figs. 10, 11, and 12. The upsurge in nanoparticle concentration profile is observed in Fig. 10 against the raising values of magnetic parameter (M). The Lorentz force produced by the enhancement of M causes a disruption in the fluid motion, which increases the thickness of the solutal boundary layer. The diminution in nanoparticle concentration profile with the increase in chemical reaction parameter (γ) and Schmidt number (Sc) is seen in Figs. 11 and 12, respectively. Physically, increase in the chemical reaction parameter (γ) accelerates nanoparticle consumption and a rise in Schmidt number (Sc) decreases mass diffusivity, resulting in a decrease in nanoparticle concentration profile.

An enhancement in the curve of M and K_p on microbial concentration profile is seen in Figs. 13 and 14, respectively. The fluctuations in M and K_p affect fluid velocity, which produces heat that increases the thickness of the microorganism boundary layer. Figure 15 illustrates the decreasing trend of microbial concentration profile in relation to the Peclet number (Pe). Increasing Pe results in

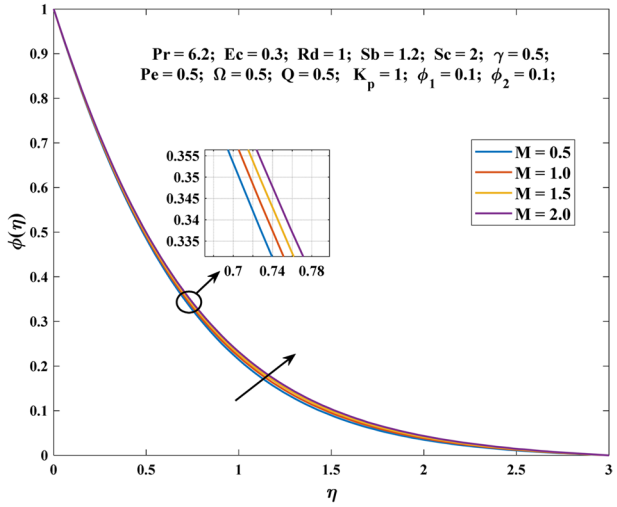

Fig. 10 Variation in $\phi(\eta)$ with M

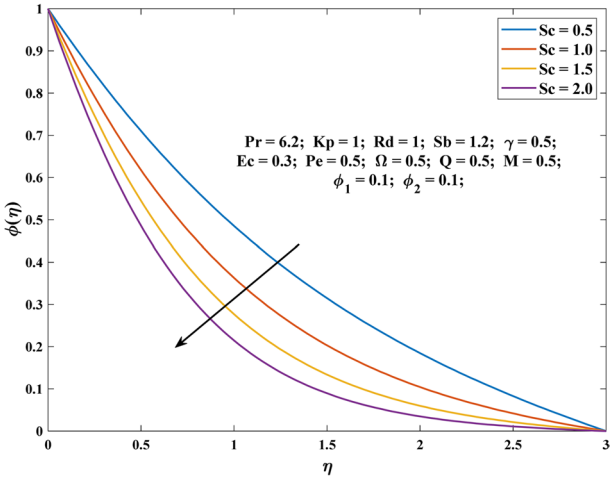

Fig. 12 Variation in $\phi(\eta)$ with Sc

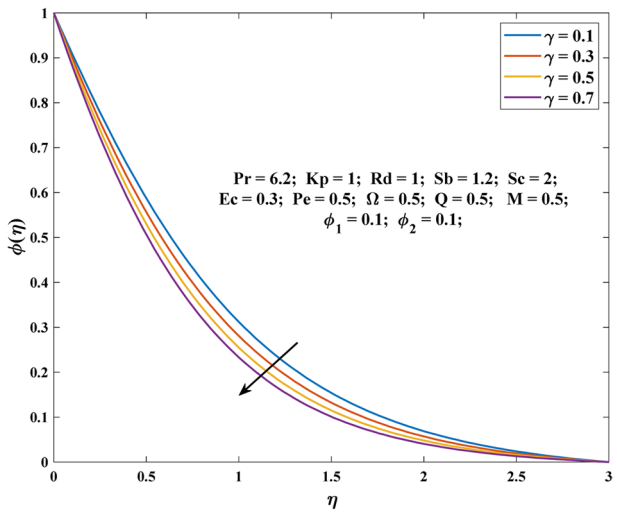

Fig. 11 Variation in $\phi(\eta)$ with γ

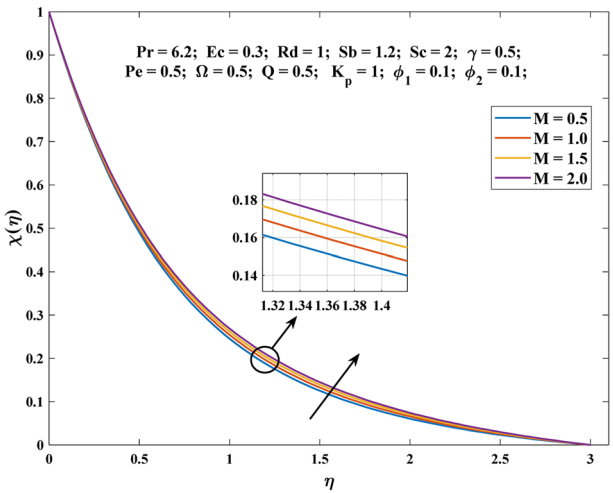

Fig. 13 Variation in $\chi(\eta)$ with M

more intense microbial movement, which reduces motile density near the surface. Higher values of the bioconvection Schmidt number (Sb) cause a decrease in the diffusivity of microorganisms, leading to reduced motile density in the fluid (this is shown in Fig. 16). Figure 17 shows variations in microbial concentration profile with respect to the microbial concentration difference parameter (σ). This declining behavior in $\chi(\eta)$ can be attributed to the fact that higher values of σ create a larger density difference between the gyrotactic microorganisms and the base fluid, causing instability on the fluid's surface and forcing the microorganisms to swim back to the fluid's bottom layer.

Tables 4, 5, 6, and 7 present the results of analyzing the effects of significant parameters on skin friction coefficient, local Nusselt number, local Sherwood number, and local motile density number.

As the amount of Cu and Al_2O_3 nanoparticles increases, along with the strength of the magnetic field and the degree of porosity in the fluid medium, the resistance to skin friction decreases (see Table 4). In other words, a higher concentration of nanoparticles, stronger magnetic field, and more porous medium lead to lower skin friction coefficient. The reason for the decrease in the skin friction coefficient as the magnetic parameter, porosity parameter, and volume fraction of copper and alumina nanoparticles increase is likely due to the properties of these materials. For example, magnetic nanoparticles may reduce the viscosity of the fluid, making it flow more easily and decreasing friction.

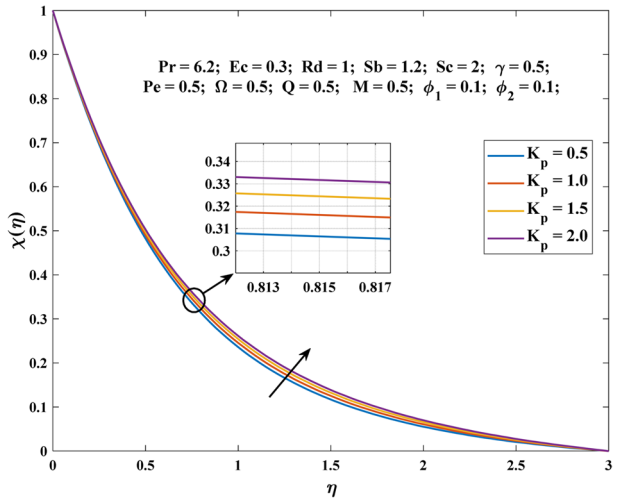

Fig. 14 Variation in $\chi(\eta)$ with K_p

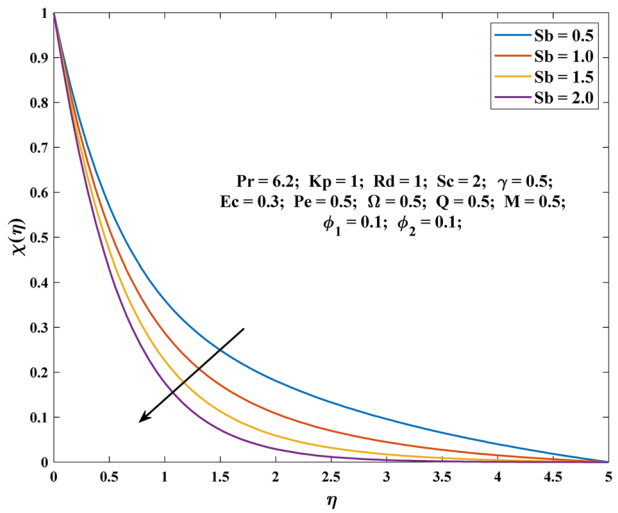

Fig. 15 Variation in $\chi(\eta)$ with Sb

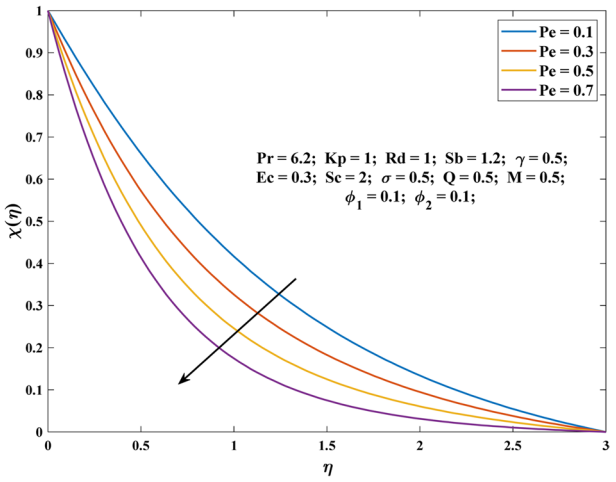

Fig. 16 Variation in $\chi(\eta)$ with Pe

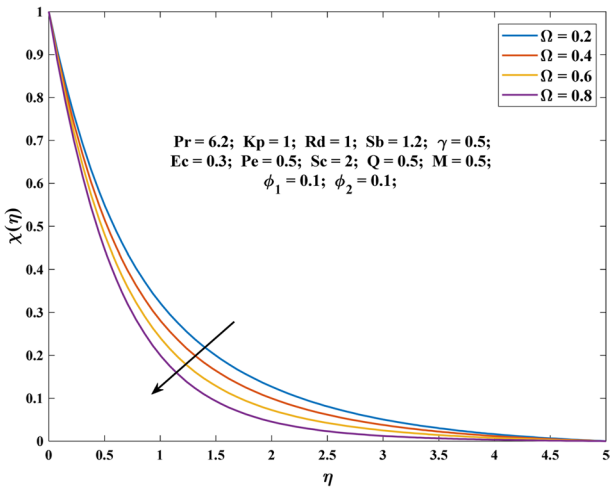

Fig. 17 Variation in $\chi(\eta)$ with σ

Similarly, the presence of nanoparticles with higher porosity and lower density can create channels and pockets in the fluid that reduce the contact area between the fluid and the solid surface, also leading to lower friction. Additionally, an increase in the volume fraction of copper and alumina nanoparticles can alter the surface characteristics of the fluid-solid interface, reducing the friction coefficient.

In Table 5, Nusselt number exhibits a contrasting behavior with respect to different parameters. An increase in the radiation parameter leads to an increase in the Nusselt number, while an increase in the magnetic and porosity parameters, as well as the Eckert number, results in a decrease in the Nusselt number. The Nusselt number is a dimensionless parameter that characterizes the convective heat transfer rate between a fluid and a surface. The behavior of the Nusselt number with respect to different parameters can be understood in terms of their influence on the convective transport of heat. An increase in the radiation parameter indicates a greater contribution of radiation to the overall heat transfer, leading to an increase in the Nusselt number. On the other hand, an increase in the magnetic parameter or porosity parameter implies an increase in the resistance to fluid flow, thereby reducing the convective heat transfer and leading to a decrease in the Nusselt number. Similarly, an increase in the Eckert number, which is a measure of the ratio of kinetic energy to thermal energy, leads to an increase in the boundary layer thickness and a reduction in the convective heat transfer, resulting in a decrease in the Nusselt number.

From Table 6, it is observed that the Sherwood number decreases with an increase in magnetic and porosity

Table 4 Variation of $Cf_xRe_x^{\frac{1}{2}}$ when $Pr=6.2$, $Ec=0.3$, $Rd=1$, $\gamma=0.5$, $Sc=2$, $Sb=1.2$, $Pe=0.5$, $\Omega=0.5$, and $Q=0.5$

M	Kp	ϕ_1	ϕ_2	$Cf_xRe_x^{\frac{1}{2}}$
0.5	1.0	0.1	0.1	−1.6404
1				−1.7933
1.5				−1.9341
0.5	0.5	0.1	1.0	−1.4802
	1			−1.6404
	1.5			−1.7863
0.5	1.0	0.01	0.1	−1.5847
		0.02		−1.594
		0.03		−1.6025
0.5	1.0	0.1	0.02	−1.6911
			0.03	−1.6858
			0.04	−1.6801

Table 6 Variation of $Sh_xRe_x^{-\frac{1}{2}}$ when $Pr=6.2$, $\phi_1=0.1$, $\phi_2=0.1$, $Rd=1$, $Ec=0.3$, $Sb=1.2$, $Pe=0.5$, $\Omega=0.5$, and $Q=0.5$

M	Kp	Sc	γ	$Sh_xRe_x^{-\frac{1}{2}}$
0.5	1.0	2.0	0.5	1.2994
1				1.2876
1.5				1.2773
0.5	0.5	2.0	0.5	1.3127
	1			1.2994
	1.5			1.2881
0.5	1.0	1.8	0.5	1.2261
		2.0		1.2994
		2.2		1.3693
0.5	1.0	2.0	0.5	1.2994
			0.6	1.3776
			0.7	1.4513

parameters, while it increases with an increase in the Schmidt number and chemical reaction parameter. These behavior is due to the fact that when the magnetic parameter increases, the velocity of the fluid decreases due to the magnetic force, which reduces the convective mass transfer rate. Therefore, as the magnetic parameter increases, the Sherwood number decreases. Similarly, when the porosity parameter increases, the available area for mass transfer decreases, and the fluid velocity also decreases. This reduction in fluid velocity reduces the convective mass transfer rate, leading to a decrease in the Sherwood number. Again, a high Schmidt number means that the momentum diffusivity is much higher than the mass diffusivity, and therefore, the mass transfer rate is slow. As the Schmidt number increases, the diffusive mass transfer rate decreases, resulting in a lower Sherwood number. Additionally, when the chemical reaction parameter increases, the rate of mass transfer increases due to the high concentration gradient caused by the fast reaction. This increase in mass transfer rate leads to a higher Sherwood number.

The motile density number exhibits an inverse relationship with the magnetic and porosity parameters, with an increase in these parameters leading to a decrease in the motile density number. Conversely, an increase in the bioconvection Schmidt number and Peclet number leads to a positive correlation with the motile density number (see Table 7). A stronger magnetic field may hinder the motility of the microorganisms and hence reduce their density. Similarly, higher porosity can facilitate the movement of microorganisms, reducing their density. Additionally, a higher Schmidt number may enhance the concentration gradient of these species, leading to an increase in motility and density. Again, a higher Peclet number means that advection dominates, which can promote the mixing and transport of microorganisms, increasing their density.

Table 5 Variation of $Nu_xRe_x^{-\frac{1}{2}}$ when $Pr=6.2$, $\phi_1=0.1$, $\phi_2=1$, $\gamma=0.5$, $Sc=2$, $Sb=1.2$, $Pe=0.5$, $\Omega=0.5$, and $Q=0.5$

M	Kp	Ec	Rd	$Nu_xRe_x^{-\frac{1}{2}}$
0.5	1.0	0.3	1.0	0.4701
1				−0.1279
1.5				−0.5776
0.5	0.5	0.3	1.0	1.2482
	1			0.4701
	1.5			0.0604
0.5	1.0	0.1	1.0	1.1687
		0.2		0.8194
		0.3		0.4701
0.5	1.0	0.3	0.5	−0.3129
			1.0	0.6581
			1.5	2.4298

Table 7 Variation of $Nn_xRe_x^{-\frac{1}{2}}$ when $Pr=6.2$, $\phi_1=0.1$, $\phi_2=1$, $Rd=1$, $Ec=0.3$, $Sc=2$, $\gamma=0.5$, $\Omega=0.5$, and $Q=0.5$

M	Kp	Sb	Pe	$Nn_xRe_x^{-\frac{1}{2}}$
0.5	1.0	1.2	0.5	1.3802
1				1.3576
1.5				1.3380
0.5	0.5	1.2	0.5	1.4055
	1			1.3802
	1.5			1.3586
0.5	1.0	1.0	0.5	1.3277
		1.2		1.3802
		1.4		1.4313
0.5	1.0	1.2	0.3	1.0436
			0.5	1.3801
			0.7	1.7215

5 Conclusion

The study covers a numerical analysis of bioconvection flow in a boundary layer for heat and mass transfer properties of hybrid nanofluid containing microorganisms over stretched porous sheets under the influence of thermal radiation and chemical reaction. To solve the nonlinear higher-order differential equation in the model, the classical Keller-Box algorithm is used after converting the higher-order ODEs into a system of first-order ODEs. The numerical analysis yielded significant findings, which are discussed in detail below.

1. The velocity profile is negatively affected by the magnetic field, while the temperature, nanoparticle concentration, and microbial concentration profiles are positively influenced by it.
2. The velocity profile exhibits a downward trend, while the temperature and microbial concentration profiles indicate an upward trend, as the porosity parameter is raised.
3. An increase in the volume fraction of copper (Cu) as well as alumina (Al_2O_3) results in a corresponding increase in the velocity profile.
4. An increase in the radiation parameter as well as Eckert number leads to a corresponding increase in the temperature profile.
5. Increase in the value of chemical reaction parameter and Schmidt number increase, there is a corresponding reduction in the concentration of nanoparticles in the hybrid nanofluid.
6. With increasing values of the Peclet number, bioconvection Schmidt number, and microbial concentration difference parameter, there is associated decrease in the concentration profile of the motile microorganisms in the hybrid nanofluid.
7. Increase in the magnetic parameter, porosity parameter, and volume fraction of copper and alumina nanoparticles results in decrease in the skin friction coefficient.
8. As the radiation parameter increases, the Nusselt number increases, but it decreases with the increase of magnetic parameter, porosity parameter, and Eckert number.
9. The Sherwood number displays a decrease with an increase in the magnetic and porosity parameters, but it demonstrates an increase with the increase in the Schmidt number and chemical reaction parameter.
10. The motile density number decreases with higher values of the magnetic and porosity parameters, but it rises with the increase in bioconvection Schmidt number and Peclet number.

Author Contributions The authors confirm contribution to the paper as follows: study conception and figures: 1st author; analysis and interpretation of results: 2nd author; draft manuscript preparation: 1st author. All authors reviewed the results and approved the final version of the manuscript.

Data Availability Not applicable.

Declarations

Ethical Approval This research project does not involve human subjects or animal experimentation. Therefore, ethics approval is not applicable. The research conducted for this project strictly adheres to ethical guidelines and principles, ensuring the highest standards of integrity and respect for all individuals involved.

Competing Interests The authors declare no competing interests.

References

1. Choi, S. U. S., & Eastman, J. (1995). Enhancing thermal conductivity of fluids with nanoparticles. *Proceedings of the ASME International Mechanical Engineering Congress and Exposition, 66*
2. Lee, S., Choi, S. U. S., Li, S., & Eastman, J. A. (1999). Measuring thermal conductivity of fluids containing oxide nanoparticles. *Journal of Heat Transfer, 121*(2), 280–289. https://doi.org/10.1115/1.2825978
3. Buongiorno, J. (2005). Convective transport in nanofluids. *Journal of Heat Transfer, 128*(3), 240–250. https://doi.org/10.1115/1.2150834
4. Kuznetsov, A., & Nield, D. (2010). Natural convective boundary-layer flow of a nanofluid past a vertical plate. *International Journal of Thermal Sciences, 49*(2), 243–247. https://doi.org/10.1016/j.ijthermalsci.2009.07.015
5. Khan, W., & Pop, I. (2010). Boundary-layer flow of a nanofluid past a stretching sheet. *International Journal of Heat and Mass Transfer, 53*(11–12), 2477–2483. https://doi.org/10.1016/j.ijheatmasstransfer.2010.01.032
6. Makinde, O., & Aziz, A. (2011). Boundary layer flow of a nanofluid past a stretching sheet with a convective boundary condition. *International Journal of Thermal Sciences, 50*(7), 1326–1332. https://doi.org/10.1016/j.ijthermalsci.2011.02.019
7. Ishak, A. (2011). MHD boundary layer flow due to an exponentially stretching sheet with radiation effect. *Sains Malaysiana, 40*(4), 391–395
8. Hayat, T., Shafiq, A., Alsaedi, A., & Shahzad, S. A. (2016). Unsteady MHD flow over exponentially stretching sheet with slip conditions. *Applied Mathematics and Mechanics, 37*(2), 193–208. https://doi.org/10.1007/s10483-016-2024-8
9. Muntazir, R. M., Mushtaq, M., Shahzadi, S., & Jabeen, K. (2021). MHD nanofluid flow around a permeable stretching sheet with thermal radiation and viscous dissipation. *Proceedings of the Institution of Mechanical Engineers, Part C: Journal of Mechanical Engineering Science, 236*(1), 137–152. https://doi.org/10.1177/09544062211023094
10. Rao, S., & Deka, P. (2023, February 8). A numerical study on heat transfer for MHD flow of radiative casson nanofluid over a porous stretching sheet. *Latin American Applied Research - an International Journal, 53*(2), 129–136. https://doi.org/10.52292/j.laar.2023.950

11. Rao, S., & Deka, P. (2022). A numerical solution using EFDM for unsteady MHD radiative Casson nanofluid flow over a porous stretching sheet with stability analysis. *Heat Transfer, 51*(8), 8020–8042. https://doi.org/10.1002/htj.22679
12. Rao, S., & Deka, P. N. (2022). A numerical investigation on transport phenomena in a nanofluid under the transverse magnetic field over a stretching plate associated with solar radiation. *Nonlinear Dynamics and Applications, 473–492*. https://doi.org/10.1007/978-3-030-99792-2_39
13. Alrihieli, H., Alrehili, M., & Megahed, A. M. (2022). Radiative MHD nanofluid flow due to a linearly stretching sheet with convective heating and viscous dissipation. *Mathematics, 10*(24), 4743. https://doi.org/10.3390/math10244743
14. Abdul Jawwad, A. K., Jawad, M., Nisar, K. S., Saleem, M., & Hasanain, B. (2023). Radiative transport of MHD stagnation point flow of chemically reacting Carreau nanofluid due to radially stretched sheet. *Alexandria Engineering Journal, 69*, 699–714. https://doi.org/10.1016/j.aej.2023.02.024
15. Majeed, A., Zeeshan, A., & Jawad, M. (2023). Double stratification impact on radiative MHD flow of nanofluid toward a stretchable cylinder under thermophoresis and brownian motion with multiple slip. *International Journal of Modern Physics B*. https://doi.org/10.1142/s0217979223502326
16. Majeed, A., Zeeshan, A., Jawad, M., & Alhodaly, M. S. (2022). Influence of melting heat transfer and chemical reaction on the flow of non-Newtonian nanofluid with Brownian motion: Advancement in mechanical engineering. *Proceedings of the Institution of Mechanical Engineers, Part E: Journal of Process Mechanical Engineering, 095440892211455*. https://doi.org/10.1177/09544089221145527
17. Jawad, M., Hameed, M. K., Nisar, K. S., & Majeed, A. H. (2023). Darcy-Forchheimer flow of maxwell nanofluid flow over a porous stretching sheet with Arrhenius activation energy and nield boundary conditions. *Case Studies in Thermal Engineering, 44*, 102830. https://doi.org/10.1016/j.csite.2023.102830
18. Jawad, M., & Nisar, K. S. (2023). Upper-convected flow of Maxwell fluid near stagnation point through porous surface using Cattaneo-Christov heat flux model. *Case Studies in Thermal Engineering, 48*, 103155. https://doi.org/10.1016/j.csite.2023.103155
19. Jawad, M. (2023). A computational study on magnetohydrodynamics stagnation point flow of micropolar fluids with buoyancy and thermal radiation due to a vertical stretching surface. *Journal of Nanofluids, 12*(3), 759–766. https://doi.org/10.1166/jon.2023.1958
20. Rao, S., & Deka, P. N. (2023). A study on MHD flow of SWCNT-Al2O3/water hybrid nanofluid past a vertical permeable cone under the influence of thermal radiation and chemical reactions. *Numerical Heat Transfer, Part A: Applications*, 1–21. https://doi.org/10.1080/10407782.2023.2207731
21. Rao, S., & Deka, P. N. (2023). A numerical study on unsteady MHD Williamson nanofluid flow past a permeable moving cylinder in the presence of thermal radiation and chemical reaction. *Biointerface Research in Applied Chemistry, 13*(5), 436. https://doi.org/10.33263/BRIAC135.436
22. Suresh, S., Venkitaraj, K., Selvakumar, P., & Chandrasekar, M. (2012). Effect of Al2O3–Cu/water hybrid nanofluid in heat transfer. *Experimental Thermal and Fluid Science, 38*, 54–60. https://doi.org/10.1016/j.expthermflusci.2011.11.007
23. Hayat, T., & Nadeem, S. (2017). Heat transfer enhancement with Ag–CuO/water hybrid nanofluid. *Results in Physics, 7*, 2317–2324. https://doi.org/10.1016/j.rinp.2017.06.034
24. Sundar, L. S., Sharma, K., Singh, M. K., & Sousa, A. (2017). Hybrid nanofluids preparation, thermal properties, heat transfer and friction factor – A review. *Renewable and Sustainable Energy Reviews, 68*, 185–198. https://doi.org/10.1016/j.rser.2016.09.108
25. Sarkar, J., Ghosh, P., & Adil, A. (2015). A review on hybrid nanofluids: Recent research, development and applications. *Renewable and Sustainable Energy Reviews, 43*, 164–177. https://doi.org/10.1016/j.rser.2014.11.023
26. Muneeshwaran, M., Srinivasan, G., Muthukumar, P., & Wang, C. C. (2021). Role of hybrid-nanofluid in heat transfer enhancement – A review. *International Communications in Heat and Mass Transfer, 125*, 105341. https://doi.org/10.1016/j.icheatmasstransfer.2021.105341
27. Shoeibi, S., Kargarsharifabad, H., Rahbar, N., Ahmadi, G., & Safaei, M. R. (2022). Performance evaluation of a solar still using hybrid nanofluid glass cooling-CFD simulation and environmental analysis. *Sustainable Energy Technologies and Assessments, 49*, 101728. https://doi.org/10.1016/j.seta.2021.101728
28. Sheikholeslami, M. (2022). Numerical investigation of solar system equipped with innovative turbulator and hybrid nanofluid. *Solar Energy Materials and Solar Cells, 243*, 111786. https://doi.org/10.1016/j.solmat.2022.111786
29. Kursus, M., Liew, P. J., Che Sidik, N. A., & Wang, J. (2022). Recent progress on the application of nanofluids and hybrid nanofluids in machining: A comprehensive review. *The International Journal of Advanced Manufacturing Technology, 121*(3–4), 1455–1481. https://doi.org/10.1007/s00170-022-09409-4
30. Dinarvand, S., Berrehal, H., Pop, I., & Chamkha, A. J. (2022). Blood-based hybrid nanofluid flow through converging/diverging channel with multiple slips effect: A development of Jeffery-Hamel problem. *International Journal of Numerical Methods for Heat & Fluid Flow, 33*(3), 1144–1160. https://doi.org/10.1108/hff-08-2022-0489
31. Ullah, A., Fatima, N., Alharbi, K. A. M., Elattar, S., Ikramullah, I., & Khan, W. (2023). A numerical analysis of the hybrid nanofluid (Ag+TiO2+water) flow in the presence of heat and radiation fluxes. *Energies, 16*(3), 1220. https://doi.org/10.3390/en16031220
32. Kuznetsov, A. (2010). The onset of nanofluid bioconvection in a suspension containing both nanoparticles and gyrotactic microorganisms. *International Communications in Heat and Mass Transfer, 37*(10), 1421–1425. https://doi.org/10.1016/j.icheatmasstransfer.2010.08.015
33. Safdar, R., Gulzar, I., Jawad, M., Jamshed, W., Shahzad, F., & Eid, M. R. (2022). Buoyancy force and Arrhenius energy impacts on Buongiorno electromagnetic nanofluid flow containing gyrotactic microorganism. *Proceedings of the Institution of Mechanical Engineers, Part C: Journal of Mechanical Engineering Science, 236*(17), 9459–9471. https://doi.org/10.1177/09544062221095693
34. Safdar, R., Jawad, M., Hussain, S., Imran, M., Akgül, A., & Jamshed, W. (2022). Thermal radiative mixed convection flow of MHD Maxwell nanofluid: Implementation of buongiorno's model. *Chinese Journal of Physics, 77*, 1465–1478. https://doi.org/10.1016/j.cjph.2021.11.022
35. Jawad, M., Hameed, M. K., Majeed, A., & Nisar, K. S. (2023). Arrhenius energy and heat transport activates effect on gyrotactic microorganism flowing in maxwell bio-nanofluid with nield boundary conditions. *Case Studies in Thermal Engineering, 41*, 102574. https://doi.org/10.1016/j.csite.2022.102574
36. Khan, W., & Makinde, O. (2014). MHD nanofluid bioconvection due to gyrotactic microorganisms over a convectively heat stretching sheet. *International Journal of Thermal Sciences, 81*, 118–124. https://doi.org/10.1016/j.ijthermalsci.2014.03.009
37. Khashi'ie, N. S., Arifin, N. M., Pop, I., & Nazar, R. (2021). Dual solutions of bioconvection hybrid nanofluid flow due to gyrotactic microorganisms towards a vertical plate. *Chinese Journal of Physics, 72*, 461–474. https://doi.org/10.1016/j.cjph.2021.05.011
38. Shamshuddin, M., Rajput, G. R., Jamshed, W., Shahzad, F., Salawu, S. O., Abderrahmane, A., & Patil, V. S. (2022). MHD bioconvection microorganism nanofluid driven by a stretchable plate through porous media with an induced heat source. *Waves in Random and Complex Media, 1–25*. https://doi.org/10.1080/17455030.2022.2126024

39. Jawad, M. (2023). Insinuation of Arrhenius energy and solar radiation on electrical conducting Williamson nano fluids flow with swimming microorganism: Completion of Buongiorno's model. *East European Journal of Physics, 1*, 135–145. https://doi.org/10.26565/2312-4334-2023-1-17
40. Sparrow, E. M., & Cess, R. D. (1978). *Radiation heat transfer* (Augmented Edition (1st) ed.). Routledge. https://doi.org/10.1604/9780070599109
41. Brewster, Q. M. (1992). *Thermal radiative transfer properties solutions manual*. Wiley-Interscience. https://doi.org/10.1604/9780471549222
42. Raptis, A. (1998). Radiation and free convection flow through a porous medium. *International Communications in Heat and Mass Transfer, 25*(2), 289–295. https://doi.org/10.1016/s0735-1933(98)00016-5
43. Waini, I., Ishak, A., & Pop, I. (2021). Radiative and magnetohydrodynamic micropolar hybrid nanofluid flow over a shrinking sheet with Joule heating and viscous dissipation effects. *Neural Computing and Applications, 34*(5), 3783–3794. https://doi.org/10.1007/s00521-021-06640-0
44. Cebeci, T., & Bradshaw, P. (1998). *Physical and computational aspects of convective heat transfer*. Springer Study Edition. Springer. https://doi.org/10.1007/b3711010.1007/978-1-4612-3918-5
45. Wang, C. Y. (1989). Free convection on a vertical stretching surface. *ZAMM-Journal of Applied Mathematics and Mechanics/Zeitschrift für Angewandte Mathematik und Mechanik, 69*, 418–420.
46. Waini, I., Ishak, A., & Pop, I. (2019). Unsteady flow and heat transfer past a stretching/shrinking sheet in a hybrid nanofluid. *International Journal of Heat and Mass Transfer, 136*, 288–297. https://doi.org/10.1016/j.ijheatmasstransfer.2019.02.101

Terms and Conditions

Springer Nature journal content, brought to you courtesy of Springer Nature Customer Service Center GmbH (“Springer Nature”).
Springer Nature supports a reasonable amount of sharing of research papers by authors, subscribers and authorised users (“Users”), for small-scale personal, non-commercial use provided that all copyright, trade and service marks and other proprietary notices are maintained. By accessing, sharing, receiving or otherwise using the Springer Nature journal content you agree to these terms of use (“Terms”). For these purposes, Springer Nature considers academic use (by researchers and students) to be non-commercial.
These Terms are supplementary and will apply in addition to any applicable website terms and conditions, a relevant site licence or a personal subscription. These Terms will prevail over any conflict or ambiguity with regards to the relevant terms, a site licence or a personal subscription (to the extent of the conflict or ambiguity only). For Creative Commons-licensed articles, the terms of the Creative Commons license used will apply.
We collect and use personal data to provide access to the Springer Nature journal content. We may also use these personal data internally within ResearchGate and Springer Nature and as agreed share it, in an anonymised way, for purposes of tracking, analysis and reporting. We will not otherwise disclose your personal data outside the ResearchGate or the Springer Nature group of companies unless we have your permission as detailed in the Privacy Policy.
While Users may use the Springer Nature journal content for small scale, personal non-commercial use, it is important to note that Users may not:

1. use such content for the purpose of providing other users with access on a regular or large scale basis or as a means to circumvent access control;
2. use such content where to do so would be considered a criminal or statutory offence in any jurisdiction, or gives rise to civil liability, or is otherwise unlawful;
3. falsely or misleadingly imply or suggest endorsement, approval , sponsorship, or association unless explicitly agreed to by Springer Nature in writing;
4. use bots or other automated methods to access the content or redirect messages
5. override any security feature or exclusionary protocol; or
6. share the content in order to create substitute for Springer Nature products or services or a systematic database of Springer Nature journal content.

In line with the restriction against commercial use, Springer Nature does not permit the creation of a product or service that creates revenue, royalties, rent or income from our content or its inclusion as part of a paid for service or for other commercial gain. Springer Nature journal content cannot be used for inter-library loans and librarians may not upload Springer Nature journal content on a large scale into their, or any other, institutional repository.
These terms of use are reviewed regularly and may be amended at any time. Springer Nature is not obligated to publish any information or content on this website and may remove it or features or functionality at our sole discretion, at any time with or without notice. Springer Nature may revoke this licence to you at any time and remove access to any copies of the Springer Nature journal content which have been saved.
To the fullest extent permitted by law, Springer Nature makes no warranties, representations or guarantees to Users, either express or implied with respect to the Springer nature journal content and all parties disclaim and waive any implied warranties or warranties imposed by law, including merchantability or fitness for any particular purpose.
Please note that these rights do not automatically extend to content, data or other material published by Springer Nature that may be licensed from third parties.
If you would like to use or distribute our Springer Nature journal content to a wider audience or on a regular basis or in any other manner not expressly permitted by these Terms, please contact Springer Nature at

onlineservice@springernature.com